

and deep average temperature of Fig. 2 to the annual behavior of the surface minimum, maximum, and average values shown in Fig. 1 (14).

Although most of the sample trench locations were chosen to be reasonably rock-free, samples were taken from under rocks at the VL2 site. These samples were modeled as a column of soil capped by a 20-cm cubical rock (15). The diurnal temperature extremes just under the rock were 201 and 230 K and lagged 1 and 6 hours, respectively, behind the exposed soil extremes. Since temperatures at this latitude are highest at the VL2 landing season, the material sampled from these locations has probably never been warmer than 234 K.

HUGH H. KIEFFER

University of California, Los Angeles

References and Notes

1. H. H. Kieffer, S. C. Chase, Jr., E. D. Miner, F. D. Palluconi, G. Münch, G. Neugebauer, T. Z. Martin, *Science* **193**, 780 (1976).
2. Analysis of the Viking soil samples by the inorganic and organic chemistry experiments and by the three biology instruments are reported in several articles in the 27 August 1976 and 1 October 1976 issues of *Science*.

3. T. A. Mutch *et al.*, *Science* **193**, 791 (1976).
4. H. Masursky and N. L. Crabill, *ibid.*, p. 809; *ibid.* **194**, 62 (1976).
5. T. A. Mutch *et al.*, *ibid.* **194**, 1277 (1976).
6. H. H. Kieffer, S. C. Chase, Jr., E. Miner, G. Münch, G. Neugebauer, *J. Geophys. Res.* **78**, 4291 (1973).
7. G. Neugebauer, G. Münch, H. H. Kieffer, S. C. Chase, Jr., E. Miner, *Astron. J.* **76**, 719 (1971).
8. The general agreement between the brightness temperatures measured in the several thermal passbands of the IRTM suggests that the surface emissivity ϵ is near unity. The difference between measured brightness temperatures and surface kinetic temperatures is approximately $[(1 - \epsilon)/4]T$ and is probably about 1 K.
9. S. L. Hess *et al.*, *Science* **193**, 788 (1976).
10. R. Arvidson, personal communication.
11. R. W. Shorthill, H. J. Moore II, R. F. Scott, R. E. Hutton, S. Liebes, Jr., C. R. Spitzer, *Science* **194**, 91 (1976); R. W. Shorthill, H. J. Moore II, R. E. Hutton, R. F. Scott, C. R. Spitzer, *ibid.*, p. 1309.
12. D. F. Winter and J. M. Saari, *Astrophys. J.* **156**, 1135 (1969).
13. A. E. Wechsler and P. E. Glaser, *Icarus* **4**, 335 (1965).
14. Thermal models to a depth of 2 m have been computed throughout the martian year for each case presented here. The detailed solution can be obtained from the author.
15. The soil column could communicate laterally to the exposed soil thermal profile. The rock had 125 thermal elements; the insolation and the radiative exchange with sunlit and shaded soil were computed separately for each face of the rock.
16. The three-dimensional thermal modeling was carried out by B. Jakosky. Financial support was provided under NASA contracts JPL-952988 and NAS 7-100.

15 November 1976

Temperatures of the Martian Surface and Atmosphere: Viking Observation of Diurnal and Geometric Variations

Abstract. Selected observations made with the Viking infrared thermal mapper after the first landing are reported. Atmospheric temperatures measured at the latitude of the Viking 2 landing site (48°N) over most of a martian day reveal a diurnal variation of at least 15 K, with peak temperatures occurring near 2.2 hours after noon, implying significant absorption of sunlight in the lower 30 km of the atmosphere by entrained dust. The summit temperature of Arsia Mons varies by a factor of nearly two each day; large diurnal temperature variation is characteristic of the south Tharsis upland and implies the presence of low thermal inertia material. The thermal inertia of material on the floors of several typical large craters is found to be higher than for the surrounding terrain; this suggests that craters are somehow effective in sorting aeolian material. Brightness temperatures of the Viking 1 landing area decrease at large emission angles; the intensity of reflected sunlight shows a more complex dependence on geometry than expected, implying atmospheric as well as surface scattering.

We report here several examples of martian thermal and reflection behavior as observed with the Viking infrared thermal mapper (IRTM): diurnal variation of atmospheric temperatures in a narrow latitude band; the thermal character of a high-altitude region and several typical craters; and the angular dependence of thermal and reflection properties at the Viking 1 (VL1) landing site. These studies were made possible by release of the lander capsule from the Viking 1 orbiter and by the asynchronous periods of both the Viking 1 and Viking 2 orbiters. First results from this investigation were reported previously (1). Additional studies of the north polar cap and landing site

surface characteristics appear separately in this issue. Although a large amount of data has been received, thus far it has been possible to do only preliminary analyses of selected areas. The following discussion is intended to demonstrate some of the more obvious examples of how Mars differs from expectations prior to the Viking missions. Since a day on Mars is 3 percent longer than a day on Earth, the time terminology can be confusing. Throughout this report, local time of day is measured in units of 1/24 of a martian solar day, designated H, and is referenced to midnight.

Atmospheric temperatures. The 15- μ m channel measures the thermal emis-

sion of atmospheric CO₂. Weighting functions for air masses between 1.0 and 6.0 are shown in Fig. 1 (2). Since our first report (1) global atmospheric temperatures have continued to show a strong latitudinal dependence in southern latitudes and diurnal variation as the predominant effect in the north. There is no evidence to date of fine spatial structure in the 15 μ m brightness temperature (T_{15}) that would indicate the entrainment of dust by local dust storms to the pressure levels which are sampled. The decrease in T_{15} toward the limb (limb darkening), caused by the sampling of higher altitudes for oblique viewing, complicates the separation of the diurnal and latitudinal effects; deconvolution has been applied in one case to separate the diurnal variation in a latitude band.

A large amount of data on atmospheric temperatures in the +40° to +55° latitude band was acquired during site selection for the second Viking lander (VL2). Direct measurement of the vertical temperature profile during lander entry (at 9 H, 3 September 1976) resulted in the classic combination of remote global sensing and "ground truth," and provided an accurate means of correcting the global data for limb darkening and thus deriving the magnitude and phase of the diurnal variation. The entry temperature profile for VL2 is shown in Fig. 2. Wave structure evident above 20 km has been interpreted in terms of thermal tides (3). Based on the inferred smooth mean profile (4) above 20 km and the measured profile below that level, a prediction was made for the T_{15} values that would be measured with the IRTM at different air masses. This modeling incorporated the broadening of weighting functions that results from the finite size of the IRTM field of view. The predicted values were found to follow closely the function:

$$T_x = T_{1.0} X^{-0.027} \quad (1)$$

where X is the air mass. This function was applied to measured T_{15} values in the data from revolutions 5 to 15 of the Viking 2 orbiter (13 to 24 August 1976) to reduce them to air mass 1.0. Reduced temperatures from the latitude band +46° to +50°, involving an average air mass correction of 1.5 K, show a marked diurnal variation (Fig. 3). The data are fit well by a sinusoid having the expression:

$$T_{15}(t) = 175 + 10 \cos \left(\frac{\pi t}{12} - 3.74 \right) \quad (2)$$

where t is in H units. Although 15/24 of the day is covered, it is possible that a minimum is reached near dawn (~4.5 H) and that the true minimum is not as

low as the 165 K the sinusoid implies. The maximum of 185 K occurs at 14.2 H. The scatter in the data is consistent with the noise in the narrow-band 15- μm channel.

The diurnal variation is at least 15 K. Because of the broad weighting function, the level at which the temperature excursion occurs is uncertain. If the atmosphere below 17 km were unchanging, a diurnal tide wave having maximum amplitude at the weighting function peak (0.58 mbar) and a half-wavelength equal to the weighting function half-width would need to have 37 K peak-to-peak amplitude. Such a wave amplitude is inconsistent with those seen in the VL2 entry profile below 40 km (Fig. 2). Moreover, the wavelength of the observed diurnal tide is short compared to the extent of the weighting function, so that the T_{15} variation would be much less than the wave amplitude.

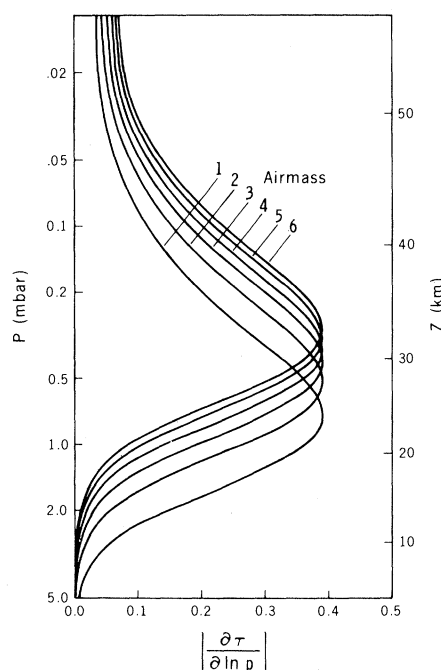
The observed variation probably arises in the lower atmosphere, where convection, infrared absorption by the gas, and direct solar heating of dust drive atmospheric temperatures to some undetermined level. The radiative-convective models of Gierasch and Goody (5) show only mild diurnal temperature variations above 5 km; the most extreme profiles given in their work would produce an amplitude of only 2 K in T_{15} . The presence of dust particles at higher levels could provide the radiative coupling to the solar flux sufficient to cause large diurnal variations in the lower atmosphere. The observed phase of maximum temperature is consistent with heating by insolation. Convective models predict a maximum at a later time of day, near 16 H (5).

In order to reproduce the observed variation in T_{15} , we have generated model temperature profiles that are constrained by the mean entry profile of VL2 at high altitudes (above 35 km) and by measurements in situ of near-surface air temperature. The daily minimum and maximum temperatures found in the lander meteorology experiment were about 190 K and 240 K and these temperatures are highly repeatable (6). These boundary conditions were used to generate profiles that fit the observed T_{15} minimum and maximum values of 170 and 185 K. The high-temperature profile was constructed by extending a linear profile to meet the mean entry curve. Since a linear profile from that level to the near-surface minimum at 190 K did not give a low enough T_{15} , the low-temperature curve was developed as a two-part profile, the upper portion being isothermal (see Fig. 2, curves a and b). This model clearly im-

Table 1. Dependence of atmosphere optical depth on ensemble dust emissivity.

ϵ	τ
0	0.10
0.20	0.14
0.50	0.21
0.75	0.26
1.00	0.32

plies that much more lower-atmosphere heating occurs than has been thought likely. Observations of twilight atmospheric brightness from the VL2 imaging experiment (7) indicate that dust is present up to at least 30 km. If the mechanism of sunlight absorption by dust is operating over a large range of altitudes, wide temperature excursions similar to those in Fig. 2 probably occur.



The introduction of profiles with shapes different from that of the entry profile will, in general, alter the form of the implied correction for air mass. However, curves a and b of Fig. 2 are not sufficiently different to require modification of Eq. 1. A time-dependent correction incorporating those profiles would yield at most an increase of 2 K in the diurnal amplitude.

Given this lower-atmosphere diurnal variation, and given that the energy source is absorption of sunlight by dust, we may estimate the implied optical depth. Since a large temperature swing near the surface is adequately explained by convection and radiative coupling with the surface, we estimate the energy contribution of those effects and derive an optical depth corresponding to the remaining energy requirement.

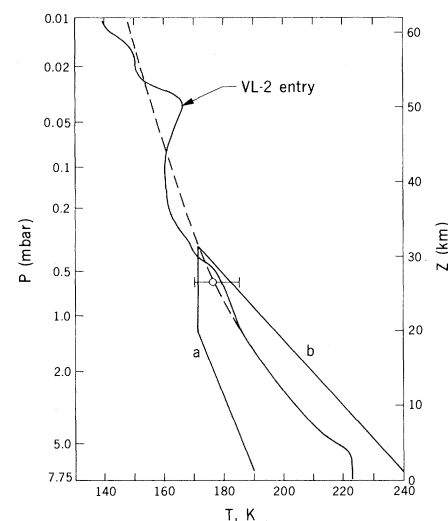


Fig. 1 (left). Weighting functions for the IRTM 15- μm channel, for observations at several air masses. Fig. 2 (right). Atmospheric temperature profiles. The VL2 entry measurement is indicated. Dashed line (---) is the inferred mean diurnal profile above 20 km.

Lines a and b are model profiles which are consistent with the observed T_{15} variation at +48° latitude and with the daily air temperature extremes recorded in the VL2 meteorology experiment. The open circle is the T_{15} measurement appropriate to the time of lander entry, with the diurnal range of T_{15} indicated by bars (-O-).

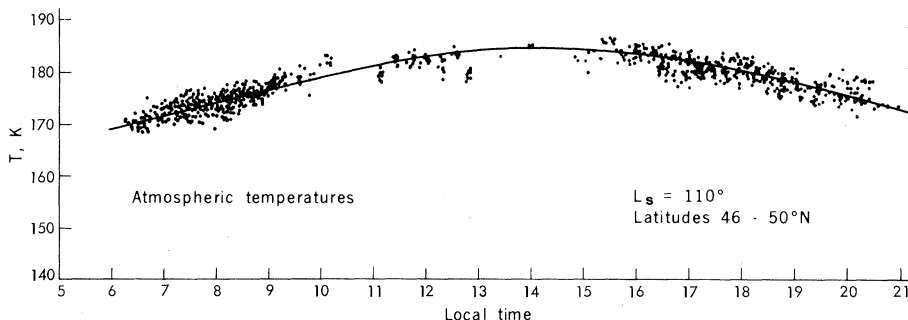


Fig. 3. Diurnal variation in atmospheric temperature at +48° latitude. Data points are the corrected T_{15} values collected during orbits 5 to 15 of the Viking 2 orbiter, 13 to 24 August 1976. The mean air mass correction was 1.5 K. The solid curve represents the best fitting harmonic function (Eq. 2).

Let W be the energy needed to induce a temperature change ΔT in the mass of gas M in a vertical column of unit area and height 28.8 km (above the 6.1-mbar

surface). This energy also supports the differential black-body radiation of that mass between the initial and final temperatures. We consider a time period be-

tween dawn and the time of maximum temperature. The temperature change used is the density-weighted difference between curves a and b of Fig. 2; a constant density scale height of 9.9 km was used. The energy is given by

$$W = \Delta T (C_p M + 4\epsilon\sigma T^3 \Delta t) \quad (3)$$

where C_p is the specific heat of CO_2 , ϵ is the ensemble dust emissivity, σ is the Stefan-Boltzmann constant, Δt the aforementioned time period, and T the density- and Planck-weighted mean temperature of the gas mass M . The profile is assumed to progress linearly from a to b over the time Δt .

With these values: $M = 12.83 \text{ g cm}^{-2}$, $C_p = 7.7 \times 10^6 \text{ erg g}^{-1}$, $\Delta T = 32.6 \text{ K}$, $T = 201 \text{ K}$, and $\Delta t = 10.4 \text{ hours}$,

$$W = 3.22 \times 10^9 (1 + 0.7 \epsilon) \text{ erg cm}^{-2} \quad (4)$$

The incident solar flux at the top of the atmosphere over the same time period is $I_0 = 1.23 \times 10^{10} \text{ erg cm}^{-2}$.

From diurnal profiles generated by Gierasch and Goody (5) we estimate that the energy supplied by the surface to the lower 5 km of a clear atmosphere is $2 \times 10^9 \text{ erg cm}^{-2}$. The remaining energy is $1.2 \times 10^9 (1 + 1.9 \epsilon) \text{ erg cm}^{-2}$, which is related to optical depth, τ , according to

$$\tau = \ln (I_0 / (I_0 - W)) \quad (5)$$

in which dust absorption of reflected sunlight and of surface thermal emission is ignored. The dependence of optical depth upon the ensemble dust emissivity is shown in Table 1.

The absorption optical depths obtained in this fashion are not inconsistent with the extinction optical depth of 0.25 found by the VL2 lander imaging experiment (7). If one also considers the aforementioned lander observation of the vertical dust distribution, it is reasonable that dust absorption of solar energy is responsible for the observed temperature variation.

Arsia Mons and the South Tharsis Upland. Brightness temperature measurements of Arsia Mons and the surrounding region before dawn and in the morning and afternoon are significantly different from those expected for an average Mars defined by Mariner 9 radiometry (8). The difference between the observed $11 \mu\text{m}$ brightness temperature (T_{11}) and the calculated Mars average model (T_m) has been mapped for mid-morning and late afternoon measurements (see Fig. 4). The Mars average model is characterized by a bolometric albedo, $A = 0.25$, and a thermal inertia, $I = 0.0065 \text{ cal cm}^{-2} \text{ sec}^{-1/2} \text{ K}^{-1}$ (I). Com-

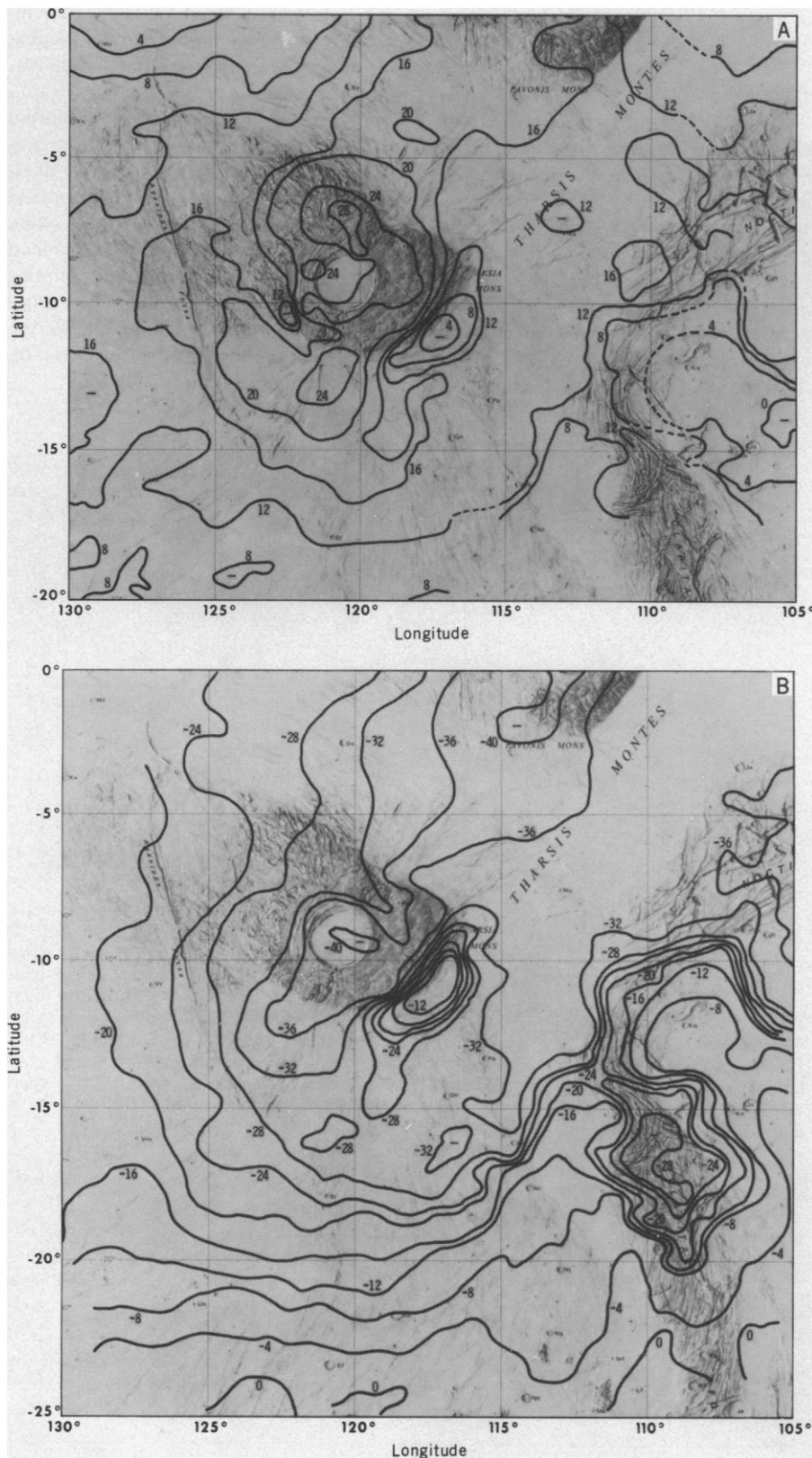


Fig. 4. Residual temperature maps for the Arsia Mons region in the midmorning (A) and late afternoon (B). The base map is the U.S. Geological Survey shaded relief map of the Phoenix Lacus quadrangle of Mars. The IRTM spatial resolution for these observations is about 40 km near the Arsia Mons caldera. Local time at longitude 120° is 9.2 H with data collected on 19 to 21 August 1976 for (A) and 17.5 H with data collected on 20 to 22 September 1976 for (B).

paring the observed brightness temperatures against such a model has the advantage of removing to first order the dependence of temperature on time of day, latitude, and season. In the midmorning nearly the entire region mapped is 10 K or more warmer than the model; the highest temperatures are found on the slopes and summit of Arsia Mons. In the late afternoon nearly the entire region is 10 K or more cooler than the Mars average model, with deviations of up to 40 K occurring at the summit of Arsia Mons.

The temperature variation for the summit caldera of Arsia Mons, including pre-dawn data, are compared with several calculated models in Fig. 5. A low value of thermal inertia is necessary to fit the observations. The surface albedo of the south Tharsis upland including Arsia Mons is not well determined because of the frequent presence of clouds. However, the argument for low inertia made here is based on the large diurnal variation observed and is to first order independent of the surface albedo. As has been pointed out in connection with Mariner 9 observations of this region (8), a decrease in inertia is expected with increasing altitude since the thermal conductivity of divided material partially depends on the gas pressure in the interparticle pore space. For the range of pressures of interest here, the thermal inertia would vary roughly as the fourth root of the gas pressure. If one takes the atmospheric pressure at the Arsia Mons caldera as 0.6 mbar (corresponding to an altitude of 27 km), this implies that the inertia of materials would decrease by a factor of 1.8 from their value at zero altitude. This would explain about a third of the observed predawn $T_{20} - T_m$ residual.

One feature of the observations presented in Fig. 5 represents a deviation from the calculated low inertia model behavior: the delayed response to sunrise and the steepness of the temperature rise from 7.5 to 9.2 H. This feature can be explained by postulating a two-component surface model in which the dominant component by area has an inertia as low as $I = 0.0005$. This surface component would drop to the CO_2 frost point at 134 K several hours before dawn and retain the resulting frost deposit for some time after dawn, whereupon this surface component would quickly heat and become the principal flux source. Regional or local slopes could be proposed to cause an apparent phase shift with respect to predictions for flat-lying terrain; a west facing slope of more than 4° over a substantial portion of the caldera would be required, but would then result in af-

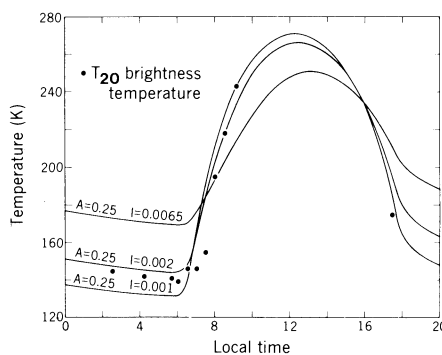


Fig. 5. The observed $20\ \mu\text{m}$ brightness temperature (solid circles) for the summit caldera of Arsia Mons, and calculated model temperatures (—). A is the bolometric albedo, and I is the thermal inertia (in units of $\text{cal cm}^{-2} \text{sec}^{-1/2} \text{K}^{-1}$). CO_2 frost condensation has been excluded in the model calculations.

ternoon temperatures being higher than observed. A systematic pattern of local slopes presenting shadowed faces to the IRTM could produce the observed delay, but no evidence exists for such special geometry. Whether or not the suggested two-component model is correct, the low predawn and afternoon temperatures are clearly associated with low inertia material in the summit caldera of Arsia Mons.

Much of the south Tharsis upland must also contain material with relatively low inertia since it heats more quickly in the morning and cools more rapidly in the afternoon than an average Mars area. Most of the region shown in Fig. 4 is between 5 km and 10 km altitude (9), but the decreased ambient pressure can account for only a small part of this inferred lower thermal inertia. Indeed, a region of moderately cratered plains near

$-12.5, 108^\circ\text{W}$, at an elevation greater than 9 km, has a thermal behavior only moderately different from the Mars average. At an even greater elevation near Arsia Mons there is another region ($-11^\circ, 117.5^\circ\text{W}$) which shows far less unusual thermal behavior than does the bulk of the south Tharsis upland. Thus the south Tharsis upland is characterized by low inertia material. Low thermal inertia requires the presence of finely divided or extremely porous material. The higher elevations in the Tharsis upland favor selective deposition of the finer material raised by dust storms; also, aeolian removal of this dust is more difficult because of the lower atmospheric pressure. Alternatively, extrusion of lavas at these low pressures could result in a frothy surface because of the expansion of included volatiles into a near vacuum.

Thermal signatures of craters in one locale. Huygens, a 450-km crater centered at $-13^\circ, 330^\circ\text{W}$ was observed by Mariner 9 to have a thermal signature which implied that the crater floor had a higher thermal inertia than did the surrounding material. Huygens and its environs have been observed by the Viking 1 orbiter at local times ranging from 1 to 10.5 H, with resolutions of 60 to 200 km; these observations allow determination of thermal inertias.

The thermal structure of the Huygens region at local times of 5 and 10.5 H has been mapped as $T_{11} - T_m$ residual temperatures (Fig. 6). The crater interior is clearly distinguishable from the immediately surrounding material. At 10.5 H, the material immediately outside of the crater walls has the highest residual temperature. This is not caused by slopes, as

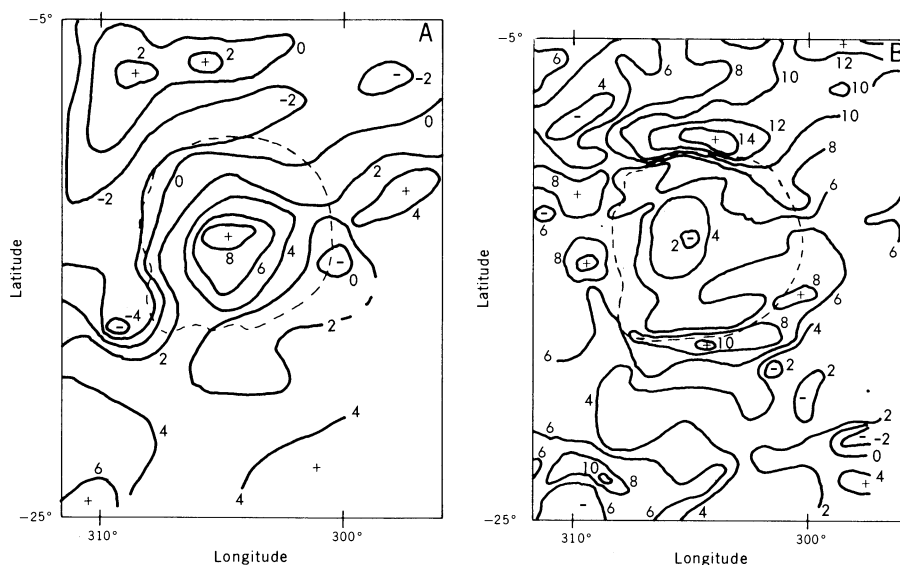


Fig. 6. Residual temperature maps of crater Huygens and environs. The contours shown represent the difference between T_{11} and T_m . The outline of the crater rim is shown as a dashed line. (A) Predawn (5 to 6 H). (B) Late morning (10 to 11 H).

these areas are clearly separated from the crater walls.

Temperatures of the floor of Huygens and the region outside the northern rim were obtained at nine different local times (Fig. 7). This latter area, within 70 km of the rim, includes the warmest material seen at 10.5 H. Measurements of reflected sunlight at this time show that the Lambert albedo (I) of the floor of Huygens varies from 0.12 to 0.15, while the albedo of all immediately surrounding material is 0.15 to 0.18. The thermal inertia was determined by fitting a thermal model to the observed temperatures and albedos. The crater floor and adjacent plain to the north have thermal inertias of 0.008 and 0.005, respectively; if one assumes the presence of uniformly sized lithic soils at 6 mbar these correspond to effective grain diameters of 0.05 and 0.015 cm (8).

Three additional nearby craters, also large enough to be resolved in the pre-dawn, have thermal inertias between 0.006 and 0.008, in each case 0.002 higher than their surroundings. The Lambert albedos of these craters are also approximately 0.02 lower than their surroundings.

There are numerous smaller craters, with diameters from 30 to 150 km, that

can be resolved only near periapsis, at local times from 10 to 16 H; at these times, temperature and thermal inertia are inversely related. Most of the crater floors are cooler than their surroundings; the remainder show no temperature contrast. While the detailed diurnal behavior has not been established, the data suggest that the floors of smaller craters also have higher inertia than does material outside the crater walls. These small craters also have relatively dark floors, so that even those with no thermal contrast probably have floors with higher inertia.

Although the consistent relative albedo and relative thermal inertia could be attributed to a consistent distribution of rocks or exposed bedrock generated during impact processes, these craters do not appear fresh and it is likely that such material has been degraded or mantled. The subdued morphology is consistent with deposition of transported material, and the thermal observations could be explained by a sorting of this material. A tentative explanation for the thermal inertia contrast across Huygens and the smaller craters is accumulation, due to entrapment, of coarse material which is more readily transported into, than out of, these craters because of the asymmet-

ric slopes of the crater walls. The observation of low albedo dune fields within southern hemisphere craters (10) provides additional evidence for such a process. The high proportion of craters which have the thermal signature described above suggests that accumulation of coarse material within craters is more prevalent than the development of identifiable dune forms.

Photometric and thermal emission functions. The determination of surface temperature and albedos by remote sensing is complicated by the dependence of measured radiant fluxes on incidence (i), emission (e), and phase (ϕ) angles of the observations (11). To compare temperatures (or visual brightnesses) obtained at different illumination and viewing conditions, the functional dependence of emergent flux on the various angles must be known. Strictly, this functional dependence varies from point to point on the planetary surface because of inhomogeneity of the surface structure. Furthermore, surface or atmospheric condensates or other sources of atmospheric opacity cause secular variations in the functional dependence even at a single surface location.

Observations intended to lead to a partial empirical determination of the angu-

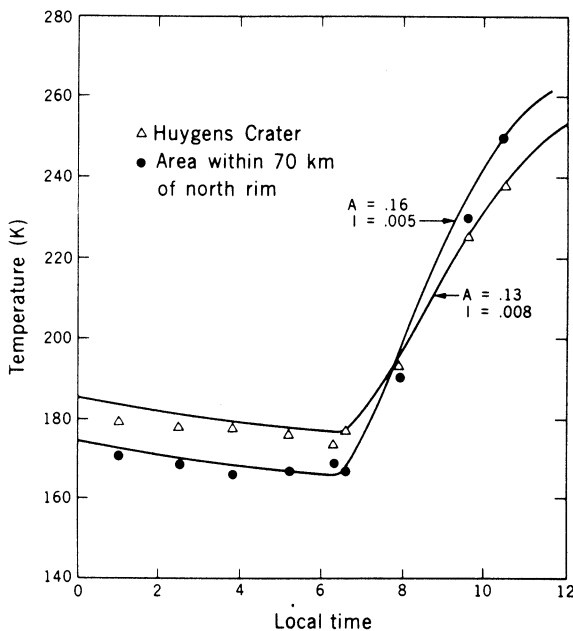
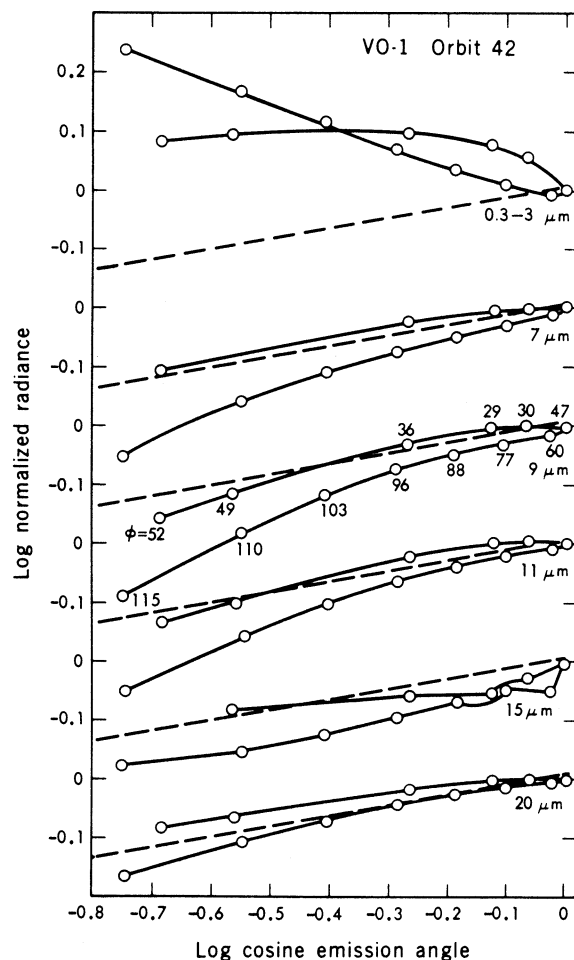


Fig. 7 (left). Morning temperatures of crater Huygens and environs. Model temperature behavior is shown for two choices of thermal inertia (I) and albedo (A); I is in units of $\text{cal cm}^{-2} \text{sec}^{-1/2} \text{K}^{-1}$. Fig. 8 (right). Observations of the VL1 area in six wavelengths at a variety of emission and phase angles. The phase angles for the observations are indicated along the $9 \mu\text{m}$ observations. The dashed lines represent radiance $\sim \cos^{0.18}e$ and are shown for comparison. Note that each curve has its own origin along the ordinate.



lar dependencies were made by the Viking 1 orbiter during revolution 42 (1 August 1976). The VL1 site was viewed repeatedly, with emission angles varying from 78° to 4° and back to 80°; the phase angle varied from 52° down to 29° and back to 115°. Since the observations were made in a relatively short time, solar incidence angles varied by only 8°, from $i = 43.4^\circ$ to $i = 51.4^\circ$. The predicted temperature variation during this time has been removed. Reflected brightnesses were corrected by assuming they vary approximately as $\cos i$. The data are shown in Fig. 8 for each of the six IRTM passbands.

An approximate fit to the temperature data is obtained by assuming a functional dependence of the form:

$$R_e = R_0 \cos^{\beta} e \quad (6)$$

where R_e is the radiance observed at a given emission angle, and R_0 is the corresponding value for vertical viewing. Values of β derived for the Moon (12) and Mercury (13) are near 0.2. Crude measurements of β ($= 0.14 \pm .07$ at $20 \mu\text{m}$) were obtained for Mars by comparing observations of the same area made several days apart by Mariners 6 and 7 (14). Unpublished data from Mariner 9 yield a β of 0.2 ± 0.1 at $20 \mu\text{m}$. The present measurements for Mars are of much higher quality than those from previous missions, and for the first time give information regarding the wavelength dependence of β . The thermal fluxes are not independent of phase angle, and are probably related to the emission angles in a more complex fashion than that expressed by the above equation. However, the data follow this relation fairly well for $e < 60^\circ$. The derived values for β for $e < 60^\circ$ and for the complete data set are given in Table 2.

The difference between values at the same emission angle may be exaggerated by a more rapid decrease in surface temperature at the local time of these observations (15.5 H) than that predicted by the simple thermal model (1, 8). However, most of the difference must be due to a real dependence of apparent brightness temperature on phase angle. One possible explanation for such a phase angle dependence would be the presence of a significant number of surface rocks at the VL1 landing site (15). If the rocks were comparable to or larger than the thermal skin depth ($\sim 20 \text{ cm}$), their sun-facing sides would be warmer than the sides facing away from the sun and the measured brightness temperature would decrease with increasing phase angle. Calculations based on a simple model with ~ 10 percent block coverage give a

Table 2. Emission angle coefficients for VL1.

Wavelength	$\beta(e < 60^\circ)$	$\beta(e \leq 80^\circ)$
7 μm	0.18	0.27
9 μm	0.20	0.32
11 μm	0.17	0.27
15 μm	0.21	0.21
20 μm	0.12	0.18

phase angle dependence comparable in magnitude with that observed (16).

The data for $15 \mu\text{m}$ are noisier than the data from the other passbands. A phase angle dependence for atmospheric emission is not expected. The difference in $15 \mu\text{m}$ brightness temperature between $\phi = 49^\circ$ and $\phi = 110^\circ$ is 4.7 K. Though each represents the average of a large number of measurements, the zero levels are determined by single measurements. The 4.7 K difference thus represents $\pm 1.5 \sigma$ from a mean value, and the apparent phase angle dependence may therefore be spurious.

If one expresses the emission angle dependence of the $15\text{-}\mu\text{m}$ measurements in terms of temperature and air mass as done in Eq. 1, the exponent is -0.036 ± 0.008 . This is slightly more negative than the value given for VL2, implying a steeper atmospheric thermal profile for the VL1 site. This is consistent with the measured VL1 entry profile (17).

The solar passband measurements are characterized by non-Lambertian behavior (a Lambert reflector would have no emission or phase angle dependence). The photometric function of Mars has previously been represented by a Minnaert function with phase-dependent exponents (18):

$$B_{(i,e,\phi)} = C_{(\phi)} (\cos i)^{K\phi} (\cos e)^{K\phi^{-1}} \quad (7)$$

where B is the measured brightness and $C_{(\phi)} = (1 + C_1\phi + C_2\phi^2 + C_3\phi^3)$. The present IRTM data resulted in a negligible phase-dependence of K . However, a third-power dependency in C_ϕ was found to be important. The coefficients which best fit the observations are: $K = 0.859$, and, for ϕ in degrees, $C_1 = -7.5 \times 10^{-3}$, $C_2 = +2.8 \times 10^{-5}$, $C_3 = +1.5 \times 10^{-7}$, $C_5 = +1.1 \times 10^{-11}$.

Extrapolation to normal incidence by means of this Minnaert function leads to an implausibly high geometric albedo ($0.34 \pm .02$); the phase integral (1.94) is also implausibly high. Thus Minnaert formulation is inadequate for these observations. The behavior of the reflected brightness observed at the VL1 site and the enhanced brightness observed generally at large incidence angles indicate that much of the variation is due to scattering in the martian atmosphere. A re-

peat of these observations, but at much lower incidence angles, is planned for the Viking extended mission. A combination of those data with the ones here described should permit separation of surface and atmospheric contributions to the total observed brightness.

The temperatures reported in the two preceding sections are brightness temperatures and have not been corrected for any angular dependence. However, for almost all those observations, the emission angle was less than 30° ; an angular behavior at those locations comparable to that of the VL1 area would not affect our conclusions.

HUGH H. KIEFFER
PHILIP R. CHRISTENSEN
TERRY Z. MARTIN

University of California,
Los Angeles 90024

ELLIS D. MINER
FRANK D. PALLUCONI
Jet Propulsion Laboratory, California
Institute of Technology, Pasadena 91103

References and Notes

- H. H. Kieffer, S. C. Chase, Jr., E. D. Miner, F. D. Palluconi, G. Münch, G. Neugebauer, T. Z. Martin, *Science* **193**, 780 (1976).
- The air mass is the amount of atmosphere along the viewing path normalized to vertical viewing. Detected radiance in the atmospheric channel is the integral over altitude of the product of a weighting function and the Planck function. Thus, changes in the vertical temperature profile and the viewing angle directly affect measured radiances. We thank Virgil Kunde for calculating weighting functions appropriate to the IRTM spectral response.
- A. Seiff and D. B. Kirk, *Science* **194**, 1300 (1976). See also R. W. Zurek, *J. Atmos. Sci.* **33**, 321 (1976).
- A. Seiff, personal communication.
- P. Gierasch and R. Goody, *Planet. Space Sci.* **16**, 615 (1968).
- S. L. Hess, R. M. Henry, C. B. Leovy, J. L. Mitchell, J. A. Ryan, J. E. Tillman, *Science*, **194**, 1352 (1976).
- J. B. Pollack, personal communication.
- H. H. Kieffer, S. C. Chase, Jr., E. D. Miner, G. Münch, G. Neugebauer, *J. Geophys. Res.* **78**, 4291 (1973).
- Topographic Map of Mars, M25M3 RMC* (U.S. Geological Survey, Reston, Va., 1976).
- J. A. Cutts, R. S. U. Smith, *J. Geophys. Res.* **78**, 4139 (1973).
- Incidence and emission angles are measured from vertical. The terminator between daylight and dark is represented by $i = 90^\circ$; the limb of the planet is represented by $e = 90^\circ$. Phase angle is defined as the angle between the sun and the spacecraft as viewed from the look-vector intercept with the planetary surface.
- D. Buhl, J. Welch, D. G. Rea, *J. Geophys. Res.* **73**, 5281 (1968).
- S. C. Chase, Jr., E. D. Miner, D. Morrison, G. Münch, G. Neugebauer, *Icarus* **28**, 565 (1976).
- G. Neugebauer, G. Münch, H. H. Kieffer, S. C. Chase, Jr., E. D. Miner, *Astron. J.* **76**, 719 (1971).
- T. A. Mutch, A. B. Binder, F. O. Huck, E. C. Levinthal, S. Liebes, Jr., E. C. Morris, W. R. Patterson, J. B. Pollack, C. Sagan, G. R. Taylor, *Science* **193**, 791 (1976).
- B. Jakosky, personal communication.
- A. O. Nier, W. B. Hanson, A. Seiff, M. B. McElroy, N. W. Spencer, R. J. Duckett, T. C. D. Knight, W. S. Cook, *Science* **193**, 786 (1976).
- T. E. Thorpe, *Icarus* **20**, 482 (1973).
- We thank B. Jakosky for modeling the thermal effects of surface block populations. The atmospheric section benefitted from conversations with C. Leovy and A. Seiff. Work supported by NASA contract NAS 7-100 at JPL and contract 952988 to the University of California. Additional support was received from the NASA Viking Project Office.

16 November 1976